Understanding activity trends in electrochemical dinitrogen oxidation over transition metal oxides

Samuel A. Olusegun,[†] Yancun Qi,[‡] Nishithan C. Kani,[‡] Meenesh R. Singh,[*,‡] and Joseph A. Gauthier[*,†]

[†]*Department of Chemical Engineering, Texas Tech University, Lubbock, TX 79409, USA*

[‡]*Department of Chemical Engineering, University of Illinois Chicago, Chicago, IL 60607, USA*

E-mail: mrsingh@uic.edu; joe.gauthier@ttu.edu

Abstract

Nitric acid (HNO_3) is a critical commodity chemical produced on an enormous scale via oxidation of ammonia NH_3 in the Ostwald process and, as such, is responsible for a significant fraction of global greenhouse gas emissions. Formation of nitric acid by directly oxidizing dinitrogen via the electrochemical nitrogen oxidation reaction (N2OR) is an attractive alternative but has so far largely remained elusive. Towards advancing our fundamental understanding of the limitations of the N2OR, in this article, we investigated the competitive adsorption dynamics of nitrogen (N_2) and water oxidation intermediates such as hydroxide (OH) on a range of transition metal oxides. Using density functional theory (DFT) calculations, we explore three possible N2OR mechanisms: direct adsorption and dissociative adsorption of N_2, and a Mars-van Krevelen (MvK) type mechanism involving adsorption of N_2 on a surface-bound atomic oxygen. We observed a strong linear scaling relation between the adsorption energy of N_2 and OH on the metal-terminated transition metal oxide, suggesting that under typical

highly oxidizing operating conditions for the N2OR ($U_{\mathrm{RHE}} > 1.24$ V), water oxidation intermediates such as OH are likely to dominate the surface, leading to vanishingly small coverage of adsorbed N_2. From this result, we find that direct or dissociative adsorption of N_2 is unlikely, suggesting a MvK type mechanism for the N2OR. Probing this mechanism further using DFT, we find that the reaction energetics are largely less favorable than water oxidation due to the high activation barrier for N_2 adsorption, which we find to be the rate-determining step for the process. Our experimental findings corroborate these findings, demonstrating that the majority of tested catalysts exhibited poor N2OR selectivity with a rate-determining step involving N_2 (g), primarily facilitating oxygen evolution reaction (OER). However, dynamic potential control emerged as a possible strategy to enhance N2OR activity, as it may limit OER and promote N_2 adsorption. This work underscores the challenges in achieving efficient N2OR, highlighting the need for novel catalyst designs and operational strategies, such as electrolyte engineering and dynamic potential control, to overcome the inherent kinetic and thermodynamic barriers.

Key words: Electrochemical N_2 oxidation; Electrochemical Synthesis of Nitrates; rutile oxides; Oxygen Evolution Reaction

Introduction

Nitrates and nitric acid (HNO_3) are high-volume commodity chemicals with important applications in fertilizers, pharmaceuticals, explosives, and many chemical synthesis processes.[1,2] Conventionally, the production of HNO_3 is achieved via. Ostwald process, where first NH_3 is oxidized to NO over Pt-Rh catalysts at 800-950^o C, followed by gas phase oxidation of NO to NO_2, which is then absorbed in H_2O to form HNO_3.[3,4] Both NH_3 production via Haber-Bosch process and HNO3 production via Ostwald process require extreme operating conditions, high capital investments for centralized operation, and are responsible for significant fractions of global energy consumption and carbon dioxide emissions.[5–7] However,

given over a century of engineering and process optimization, NH_3 and HNO_3 production are both extremely energy efficient, approaching thermodynamic limits.[8] Such economies of scale and efficiencies are likely to complicate decarbonization, since competing economically with conventional production will be a significant challenge, despite growing interest from public stakeholders. In light of the demand to decarbonize and the challenges faced in the production of HNO_3, new, disruptive technologies will be required.[9]

One pathway towards decarbonization of HNO_3 production involves electrochemical ammonia synthesis (EAS), which in principle, can offer a more sustainable route for the production of the NH_3 feedstock to the Ostwald process. Here, NH_3 is synthesized by electrochemically reducing N_2, utilizing electrical energy from renewable sources such as solar and wind energy to drive the reaction at more moderate conditions. Such a technology would not only reduce the carbon footprint of NH_3 production but would also facilitate decentralized production of NH_3, since it is also compatible with small-scale facilities.[10,11] Several EAS strategies are being actively investigated, including the direct electrochemical N_2 reduction reaction (N2RR) and metal (X)-mediated NH_3 synthesis (X-MAS).[12–15] However, the N2RR is to-date unfortunately limited due to the inertness of N_2, the high dissociation energy of N_2 triple bond, low solubility of N_2 in aqueous media and the unfavorable scaling leading to a dominant side reaction - Hydrogen Evolution Reaction (HER).[16–20] Given the challenges with direct electrochemical reduction of N_2, considerable attention has been driven towards the Li-mediated NH_3 synthesis pathway.[21–24] Perhaps the greatest hurdle to overcome towards economic feasibility is the overall energy efficiency of the process, which is hampered by the very reducing electroplating potential of Li (around -3V vs SHE in commonly used electrolytes), necessitating large overpotentials.[25–33]

Alternatively, the need to first synthesize NH_3 could be entirely circumvented by directly oxidizing N_2 via the electrochemical N_2 oxidation reaction (N2OR). Such a process would avoid the need to compete with the kinetically facile HER, and in aqueous media, it would instead compete with the comparatively sluggish oxygen evolution reaction (OER).

Additionally, electrochemical production of HNO_3 would, in principle, open a new pathway towards electrochemical NH_3 synthesis, since reducing nitrate to NH_3 is well-established in the literature with high activity and stability, approaching industrially relevant current densities.[34–38] However, literature reports to-date have found that, like the OER, the N2OR is kinetically slow, resulting in very poor selectivity and reaction rates towards nitrate.[39–49] Previous reports aimed at a molecular-level understanding of the limitations of N2OR suggest that activation of N_2 with adsorbed oxygen *O to form *N_2O is a possible rate-determining step. Emphasis has been placed on the need to suppress the competitive OER, which is analogous to suppressing the HER during N2RR. Prior reports have investigated Anatase and rutile oxide catalysts as candidates for the N2OR, such as TiO_2, PtO_2, PdO_2, SnO_2, Fe-based catalysts (such as AD-Fe NS), $IrSnO_2$, and others.[50–54]

In this work, we unravel the competition between OER intermediates on rutile oxide surfaces, and develop a molecular-level understanding of the possible N2OR mechanisms: direct N_2 adsorption on a metal site, dissociative adsorption of N_2, and a Mars-Van-Krevelen (MvK) type mechanism. We investigate a range of transition metal oxide surfaces, taking into consideration the relevant competing reactions and surface conditions. Using a linear scaling analysis of the reaction thermodynamics and relevant activation barriers, we investigate the feasibility of each mechanism under reaction conditions, identify regions of interest, and suggest possible techniques to improve N2OR. Utilizing the theoretical framework we established, a targeted subset of metal oxide surfaces were synthesized, characterized, and evaluated for activity and selectivity toward the N2OR. Our findings suggest that dynamic potential control may significantly improve overall selectivity towards the desired process and away from the competing OER. The insights we develop here may lead to the discovery of novel catalysts and processes for this critical reaction, towards the ultimate goal of achieving sustainable NO_3^- and NH_3 synthesis.

The remainder of this article is structured as follows: first, we outline the methods used to investigate this process (computational, synthesis, characterization, testing, including prod-

uct quantification). We then discuss the results of our investigation into competitive binding of N_2 and OER intermediates on a range of transition metal oxide surfaces, and outline the possible reaction mechanisms of the N2OR. After exploring the free energy landscape via thermodynamic linear scaling analysis and calculation of selected relevant activation barriers, we revealed that the applied potential has a significant effect on the dominant expected surface coverage. Using this new insight, we synthesize, characterize, and test a targeted subset of transition metal oxide catalysts for this process, and leverage dynamic potential control to maximize observed selectivity and activity towards the N2OR.

Methods

Computational details

Density functional Theory (DFT) in conjunction with the computational hydrogen electrode (CHE)[55] was used to calculate the adsorption energy of intermediates along the reaction pathway. Vienna Ab initio Simulation Package (VASP)[56–58] interfaced with the atomic simulation environment(ASE)[59] was used to perform all DFT calculations. For each atom, the core electrons were described using Projector augmented wave (PAW) pseudopotentials,[60] and valence electrons were expanded as planewaves up to a kinetic energy cutoff of 500 eV. The electron exchange and correlation interactions were accounted for using the revised Perdew-Burke-Ernzerhof (RPBE)[61] exchange-correlation functional by Hammer and Nørskov. Solvation effects were accounted for using a continuum solvation model as implemented in VASP (VASPsol).[62,63] A $(4 \times 4 \times 1)$ Monkhorst-Pack[64] k-point mesh was used to sample the Brillouin zone. To calculate the adsorption energies, a $(1 \times 2 \times 3)$ supercell of rutile (110) facet was used with the bottom two layers fixed and the top layer free to relax with the adsorbate. Geometries were considered to be optimized when the maximum force on each unconstrained atom fell below 0.05 eV/Å. The adsorption Gibbs free energies, ΔG

of the reaction intermediates are calculated using the expression

$$\Delta G_{ads} = \Delta E_{ads} + \Delta ZPE - T\Delta S \quad , \tag{1}$$

where ΔE is the difference in electronic energy of the adsorbed species, ΔZPE is the difference in zero-point energies, and ΔS is the change in entropy of the adsorbed species with respect to the catalyst surface. The ZPE and entropies S were calculated using the Harmonic Oscillator approximation, which assumes that adsorbed molecules vibrate harmonically and have only vibrational degrees of freedom. This approximation is valid in the limit of small molecules on strong binding surfaces;[65] in this work, we explore small molecules on a range of surfaces, including weak-binding transition metal oxides, and as such we may underestimate the entropy of the adsorbed state.

To calculate the Gibbs free energy of a reaction step, for example, the adsorption of N_2,

$$N_2 + * \longrightarrow *N_2 \quad . \tag{2}$$

The Gibbs free energy of reaction is written as;

$$\Delta G_{ads} = \Delta G_{*N_2} - \Delta G_{N_2} - \Delta G_{*} \quad , \tag{3}$$

where ΔG_{*N_2} is the Gibbs free energy for absorbed N_2, ΔG_{N_2} is the Gibbs free energy of formation of N_2 gas, and ΔG_{*} is the Gibbs free energy of the clean surface. To model the competitive adsorption step, we approximate the system as nonreactive where the adsorbed intermediates are not consumed. A competitive Langmuir adsorption model was used to calculate the coverage of each of the two competing adsorbed species at potentials between 0.0V and 2.0V vs RHE, as shown in Equations 4 and 5 below.

$$\theta_A = \frac{K_{A,eq} \times p_A}{1 + K_{A,eq} \times p_A + K_{B,eq} \times p_B} \tag{4}$$

$$K_{A,eq} = \exp\left(\frac{-\Delta G_{ads}}{k_{\mathrm{B}}T}\right) \tag{5}$$

Here θ_A is the coverage of species A on the catalyst surface, $K_{A,eq}$ is the equilibrium constant for adsorption of species A, p_A is the partial pressure of species A (or mole fraction) $\Delta G_{A,rxn}$ is the Gibbs free energy of adsorption of species A, T temperature in Kelvin and k_{B} the Boltzmann constant.

Experimental methods

Catalyst Synthesis

All the oxide catalysts were prepared by sputter coating the base metal using *EMS Q150R* sputter coater followed by oxidation in 0.1 M KOH. PtO_2 was prepared by sputter coating 10 nm of Pt on the gas diffusion layer followed by oxidation in 0.1 M KOH at 2 V vs. RHE for a period of 0.5 h. PdO_2, RuO_2, and TiO_2 were prepared using similar methods. TiO_2/PdO_2 was prepared by sputter coating 10 nm of Ti and 2 nm of Pd on the gas diffusion layer followed by oxidation in 0.1 M KOH at 2 V vs. RHE for a period of 0.5 h. TiO_2/RuO_2 was prepared using a similar procedure. The source and purity of all materials are provided in the Supporting Information (SI).

Electrochemical Measurements

All the electrochemical experiments were performed in a gas diffusion electrode (GDE) flow cell (a schematic is provided in the supporting information). 0.1 M K_2SO_4 was used as the electrolyte. A neutral pH electrolyte was used for all the studies to suppress OER and to keep the electrodes stable under oxidizing potentials. The electrolyte was pumped at 40 mL per minute. N_2 was passed in a flow-by configuration at a flowrate of 20 sccm. Excellion anion exchange membrane (*Snowpure*) was used to separate the anolyte and the catholyte side. Pt plate was used as the counter electrode. Ag/AgCl/KCl was used as the reference electrode.

The separation distance between electrodes and membrane is 2cm. The surface area of Pt plate and membrane are $3cm^2$ and $1cm^2$ for each. Chronoamperometric experiments were performed for a period of 1 h for each data point. The details of chemicals and materials used in this study are provided in the supporting information.

Product Quantification

The O_2 was quantified using Gas Chromatography. NO_3^- and NO_2^- present in the electrolyte were quantified by using the Griess Spectrometric method.[66] The experiment steps are shown in the supporting information.

NMR detection and quantification

NMR analysis was performed using a *Bruker Neo 600 MHz* system equipped with a QCI-FF cryoprobe, with dimethylsulfoxide-d6 (DMSO-d6) serving as the deuterated solvent. $^{14}N_2$ was replaced by $^{15}N_2$ for the N2OR reactions. After electrolysis, 570 μL of the electrolyte was combined with 30 μL of DMSO-d6 and transferred into an NMR tube for product quantification. A total of 32 scans were performed. For improved resolution, the excitation sculpting method was utilized, employing a 3-ms 180° shaped pulse centered at 260 ppm. The perfect-echo variant was selected to minimize J-modulation for samples analyzed at 500 MHz.

Scanning Electron Microscopy (SEM) and Energy Dispersive X-Ray Spectroscopy (EDS)

SEM and EDS analysis for pre and post-N2OR catalysts were conducted using a *Hitachi SU8030 Field-Emission SEM*. Image scans were performed at an accelerating voltage of 5 kV and an emission current of 10 µA, using varying magnifications. EDS elemental mapping and identification were carried out at an accelerating voltage of 20 kV, with signals collected from both upper and lower detectors to maximize signal acquisition.

X-Ray Photoelectron Spectroscopy (XPS)

XPS analysis for pre- and post-N2OR catalysts was done using *Thermo Scientific ESCALAB 250XI microprobe* with an Al Kα source. The beam diameter was set to an optimal value of 500 μm. Each analysis consisted of a survey scan to check for impurities and an elemental scan to access the chemical state of the catalyst. All XPS spectra were corrected for charge shift using the C1s peak at 298 eV as a reference. To ensure maximum signal-to-noise ratio, at least 10 spectra were acquired for the survey scan and 20 spectra for the individual elemental scans of Ti and Pd.

Results and Discussion

Competitive N_2 and OH Adsorption

Electrochemical N_2 oxidation can occur through three major mechanisms which include

1. direct adsorption to a metal site ($N_2 + * \longrightarrow *N_2$)
2. dissociative adsorption ($N_2 + 2* \longrightarrow 2*N$)
3. Mars–van Krevelen (MvK) mechanism ($N_2 + *O \longrightarrow *ON_2$)

Here, * refers to a vacant metal terminated site on the oxide. We investigate the viability of the first mechanism (direct adsorption to a metal site) by calculating the adsorption energy of the first intermediate of each of the two major competing reactions (OER and N2OR). The first intermediate of the OER in the typical 4-step mechanism is adsorbed hydroxide (*OH) while the first intermediate of N2OR in this mechanism is taken to be adsorbed N_2 (*N_2). The adsorption energies $E_{*\mathrm{OH}}$ and $E_{*\mathrm{N_2}}$ were calculated on a range of transition metal oxides. Using the calculated energies, we observe a linear scaling relation between the N_2 and OH binding energy with each intermediate representing the first reaction step for N_2 oxidation and OER respectively. Using the CHE to model the CPET reaction involved

in the first step of the OER, we estimated the values of the adsorption energies ($E_{*\mathrm{OH}}$ and $E_{*\mathrm{N_2}}$) at two different potentials: 0.0V and 2.0V vs RHE, with 2.0V vs RHE representing a typical operating potential for N2OR. Figure 1 shows $E_{*\mathrm{N_2}}$ against $E_{*\mathrm{OH}}$ at (a) an applied bias of 0.0V and (b) 2.0V vs RHE.

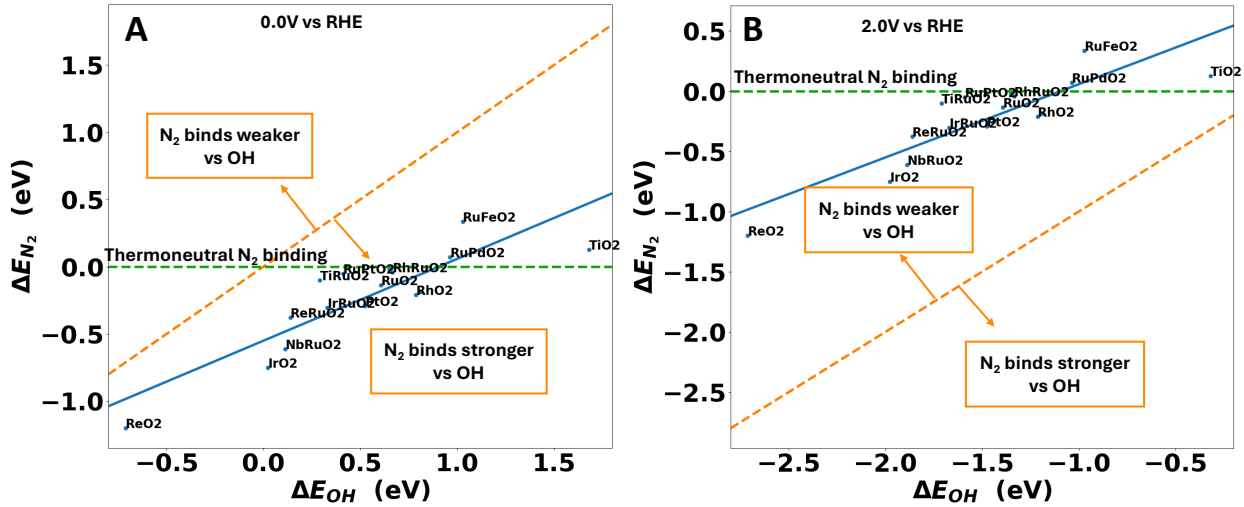

Figure 1: Scaling of $\Delta E_{\mathrm{N_2}}$ with OER intermediates (i.e., hydroxide) at (A) $U = 0$ and (B) $U = +2$ V vs RHE.

The orange parity line in Figure 1 denotes the boundary between the region of stronger OH binding and the region of stronger N_2 binding. The green horizontal line in Figure 1 denotes the line of thermoneutral N_2 binding, below which N_2 binding is exergonic and above which N_2 binding is endergonic. From Figure 1 we can observe that at low potentials (0.0V vs RHE), N_2 binds relatively stronger than OH on all the catalyst materials used. Whereas, at higher potentials (2.0V vs RHE), due to the high dependence of OH binding energy on potential, OH binds stronger on all catalyst materials tested. From these results, we infer that at N2OR operating conditions ($U > 1.24V$ vs RHE), the energetic drive towards N_2 adsorption is much lower compared to OH adsorption making direct adsorption of N_2 on a metal-terminated catalyst surface unlikely. This implies that OER intermediates are likely to dominate surface coverage on most catalyst surfaces at operating conditions, promoting OER

activity and inhibiting N2OR. In general, at a lower potential, N_2 adsorption will dominate the surface of the catalyst but lacks the driving force to complete the N2OR process. These observations are instrumental in deducing potential cycling as a viable strategy to improve N2OR activity on rutile oxides and will be explored further below.

To further understand the competitive adsorption of OH and N_2 at various reaction conditions (potential and N_2 binding energy), using the linear scaling relation between $\Delta E_{*\mathrm{OH}}$ and $\Delta E_{*\mathrm{N_2}}$ shown in Figure 1 and $\Delta E_{*\mathrm{N_2}}$ as a descriptor, we calculated the surface coverage of N_2 for a range of $\Delta E_{*\mathrm{N_2}}$ at potentials between 0.0V and 2.0V vs RHE using a competitive Langmuir adsorption model (see methods for more details). Figure 2 shows the estimated surface coverage at potentials between 0.0V and 2.0V vs RHE for a range catalyst Gibbs free energy of N_2 adsorption $\Delta G_{*\mathrm{N_2}}$.

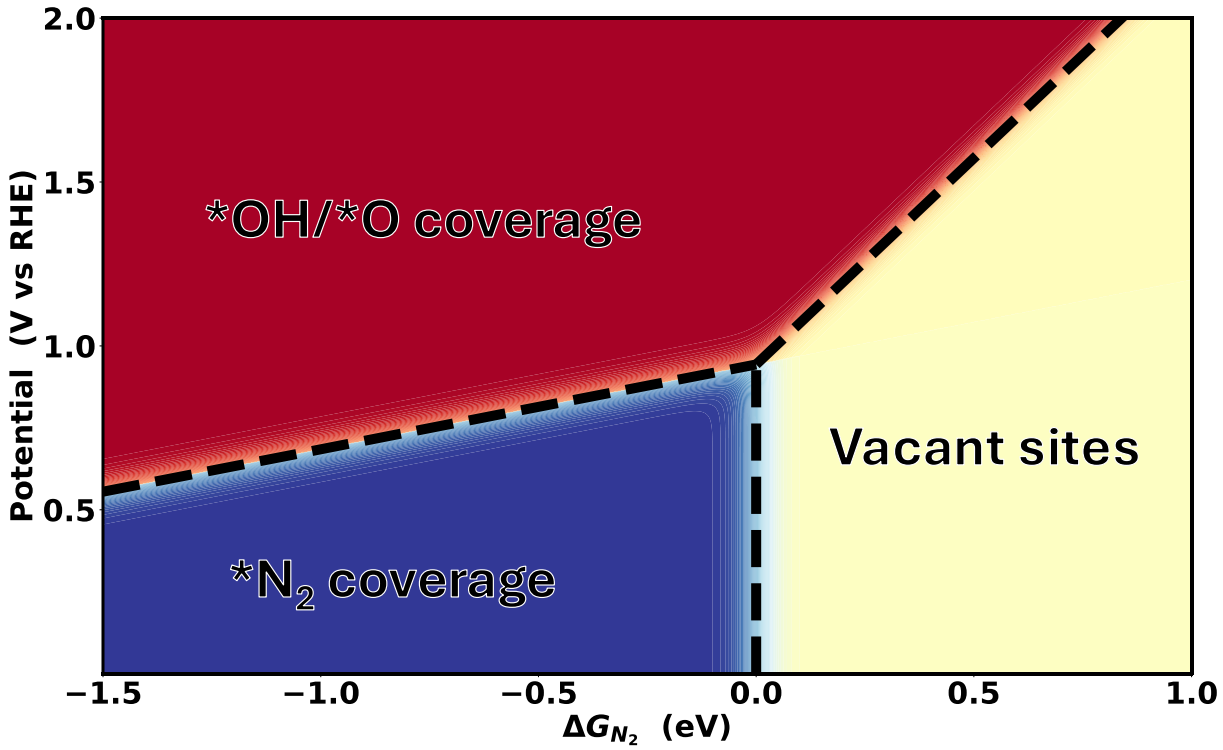

Figure 2: Regions of full monolayer coverage of (a)*N_2, (b) *OH/O, and (c) vacant sites, as a function of N_2 adsorption energy (ΔG_{N_2}) and the applied potential (V vs. RHE) during N2OR

At less oxidizing potentials, the surface coverage of N_2 is high on moderate and strong binding catalysts but, as the potential increases the driving force for N_2 adsorption is surpassed by OH adsorption energy. At operating conditions, ($U > 1.24$ V vs RHE) the surface coverage of N_2 is predicted to be close to zero. Our result may explain the very low N2OR selectivity on moderately strong binding catalysts.[50] From Figure 1 and Figure 2, we infer that a direct adsorption pathway for N2OR would likely not be competitive because of the extremely low N_2 coverage on most materials at operating conditions and the very endergonic and unstable first electrochemical step of a coupled oxidation-adsorption step, i.e. $^*N_2 + H_2O \longrightarrow ^*N_2OH + (H^+ + e^-)$. Our simulations suggest that $^*N_2OH$ is an unstable molecule, as it dissociates spontaneously when adsorbed on a single metal-terminated rutile oxide site. As shown in Figure S5, it may be stable when the two nitrogen atoms are bridged across two metal-terminated rutile oxide sites (ΔG_{rxn}=+2.1 eV on IrO_2). Given the exceptional rarity of free sites under operating conditions (not to mention the probability of two such sites being adjacent), we find this pathway to be unlikely.

Following a similar thought process, the dissociative adsorption pathway is unlikely. In addition to the rarity of free metal sites on metal oxides under operating conditions, N_2 dissociation is energetically quite unfavorable on these relatively weak-binding surfaces (ΔG_{rxn}=+3.5 eV on IrO_2). It should be noted that the conclusions we have reached here are based on the sites considered in this work (i.e., single crystal surfaces of rutile oxides); defect sites or high index facets may behave differently. However, we anticipate similar trends on such sites.

Mars Van Krevelen (MvK) mechanism

Given our findings suggesting a pathway involving the metal termination to be unlikely, an exhaustive list of possible paths through an MvK mechanism that involves the adsorption of N_2 to the oxygen-terminated oxide ($N_2 + ^*O \longrightarrow ^*ONN$) was investigated. The most probable pathway was determined using the minimum energy states from the reactants

to the desired product and relevant activation barriers. This pathway involves a series of elementary steps (chemical and electrochemical) preceded by the formation of an oxygen-terminated oxide(O^*).

$$H_2O + * \longrightarrow O^* + 2(H^+ + e^-) \tag{6}$$

The reaction above is a prerequisite for the MvK mechanism considered in this work. The overall reaction for N2OR can be written as;

$$N_2 + 6H_2O \longrightarrow 2(H^+ + NO_3^-) + 10(H^+ + e^-) \tag{7}$$

We also accounted for the possible side reactions such as; OER, N_2O, NO, and NO_2 evolution,

$$2H_2O \longrightarrow O_2 + 4(H^+ + e^-) \tag{8}$$

$$N_2 + H_2O \longrightarrow N_2O + 2(H^+ + e^-) \tag{9}$$

$$N_2 + 2H_2O \longrightarrow 2NO + 4(H^+ + e^-) \tag{10}$$

$$N_2 + 4H_2O \longrightarrow 2NO_2 + 8(H^+ + e^-) \tag{11}$$

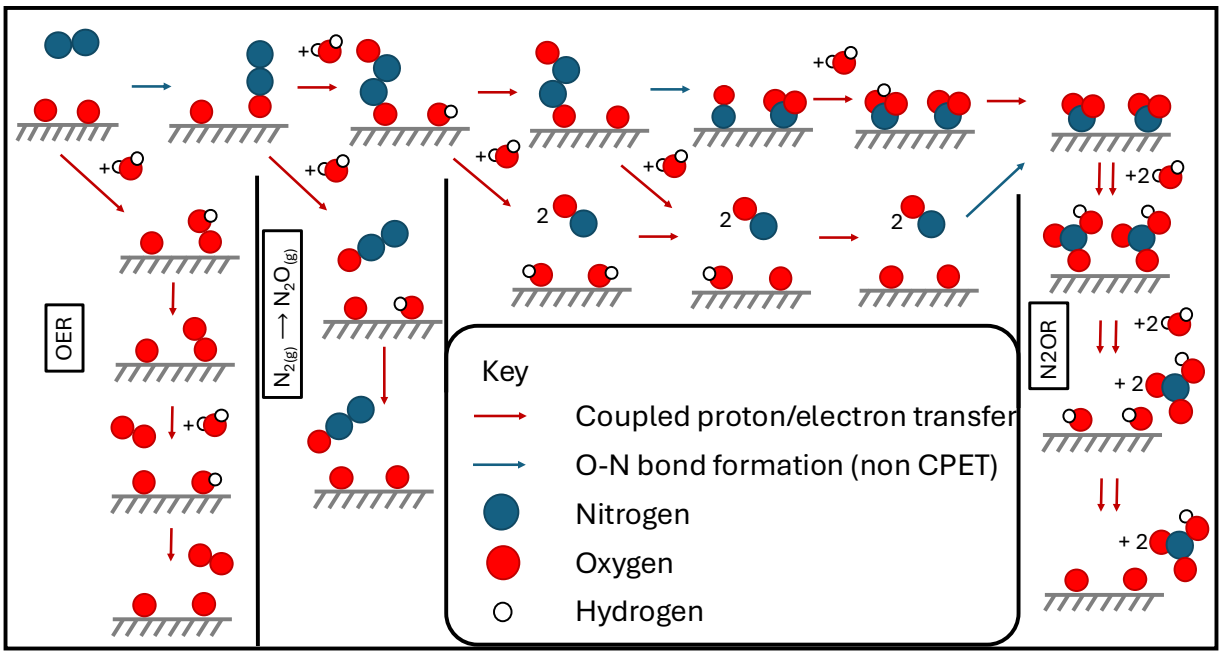

Figure 3: Schematic mechanism overview

Figure 3 shows a schematic overview of the N2OR reaction through the MvK mechanism including the major side reactions. The desired N2OR reaction includes ten CPET steps, an O-N bond formation step, and a N-N bond dissociation step. Here, O_2 gas is produced via the OER. Products such as N_2O, NO, and NO_2 can be produced due to incomplete oxidation of N_2. Such products could additionally be oxidized to nitrate through thermochemical in-solution oxidation, which may explain the low concentration of such products and may lead to a systematic underestimation of nitrate Faradaic efficiency. For the N2OR MvK mechanism to occur, N_2 must first adsorb to the oxygen-covered surface through a thermochemical Eley–Rideal-like step (N_2 + *O $\longrightarrow$ *ON_2). We find the adsorption of N_2 is largely independent of the applied potential (Figure S3 and S4) while the corresponding step in the case of OER (*O + H_2O $\longrightarrow$ *OOH + (H^+ + e^-)) is linearly dependent on the applied potential. As the applied potential increases, the O-OOH step becomes more exergonic while the N_2 adsorption energy ($\Delta G_{*ONN} - G_{*O}$) remains the same.

For N_2 activation through the MvK mechanism, the adsorption step is perhaps the most

critical step, because of the inertness of N_2 and its independence of potential. For N2OR to occur through this mechanism the adsorption step must be exergonic, or slightly endergonic, if operating at elevated temperatures. The adsorption Gibbs free energy $\Delta G_{*ONN} - G_{*O}$ was calculated on selected rutile oxides and a linear scaling relation was developed with atomic nitrogen binding energy ΔE_N. Figure 4 shows the scaling relation between $\Delta G_{*ONN} - G_{*O}$ and ΔE_N.

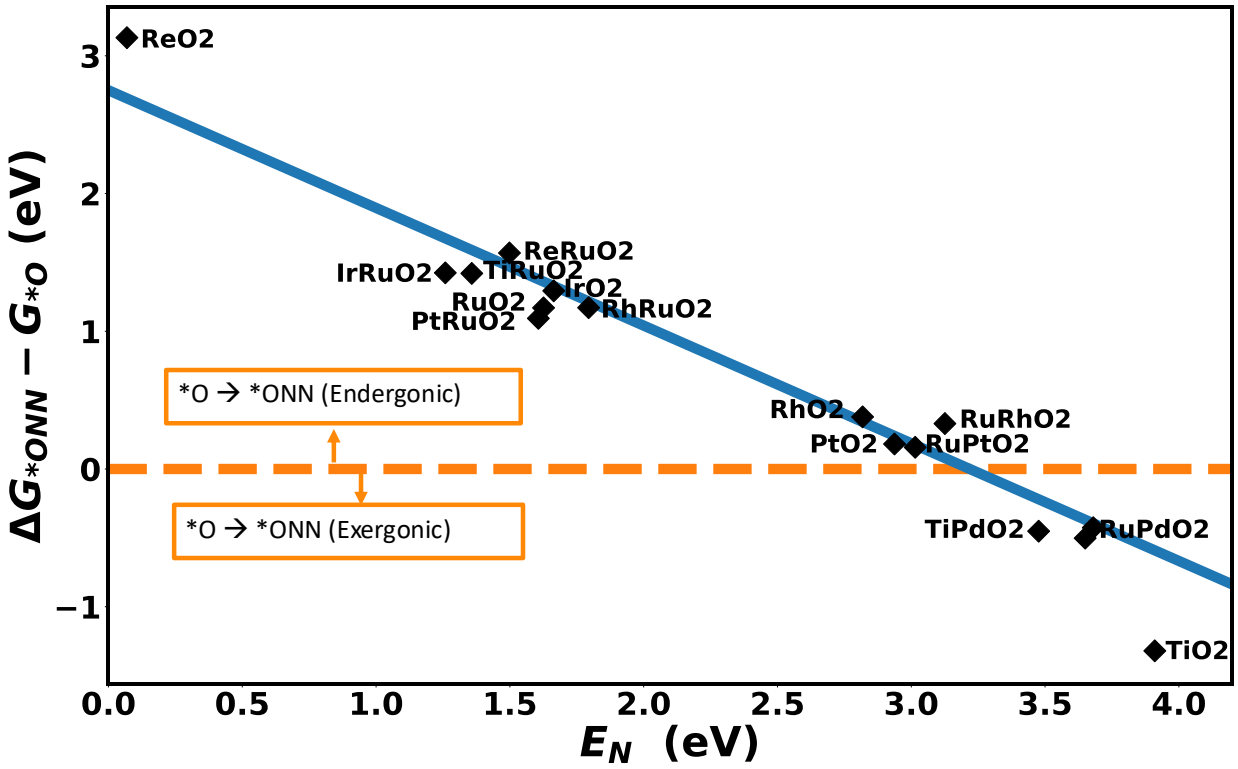

Figure 4: Linear scaling of N_2 adsorption Gibbs free energy through the MvK mechanism ($\Delta G_{*ONN} - G_{*O}$) as a function of atomic nitrogen binding energy (ΔE_N) on rutile oxides

For stronger binding rutile oxides (lower ΔE_N), N_2 adsorption to the surface oxygen is endergonic but, somewhat counter-intuitively, gradually becomes exergonic as we move towards weaker binding rutile oxides. This is likely because, in stronger binding rutile oxides, the surface oxygen is also strongly bonded, making the surface oxygen less reactive and energetically less favorable for N_2 adsorption.

To show the reaction energy of each step in the N2OR reaction, we used a bimetallic

oxide as rutile with an exergonic N_2 adsorption energy (TiPdO2). The bimetallic rutiles are achieved by replacing one surface metal in the rutile with a dopant metal. For example, in the case of TiPdO2, one surface Ti metal of the TiO2 rutile oxide is substituted with Pd metal, as shown in Figure S2. We calculated the Gibbs free energy of each step along the reaction path on TiPdO2(110) including undesired pathways. Figure 5A shows the energy diagram for N2OR reaction on TiPdO2(110) at 2V vs RHE.

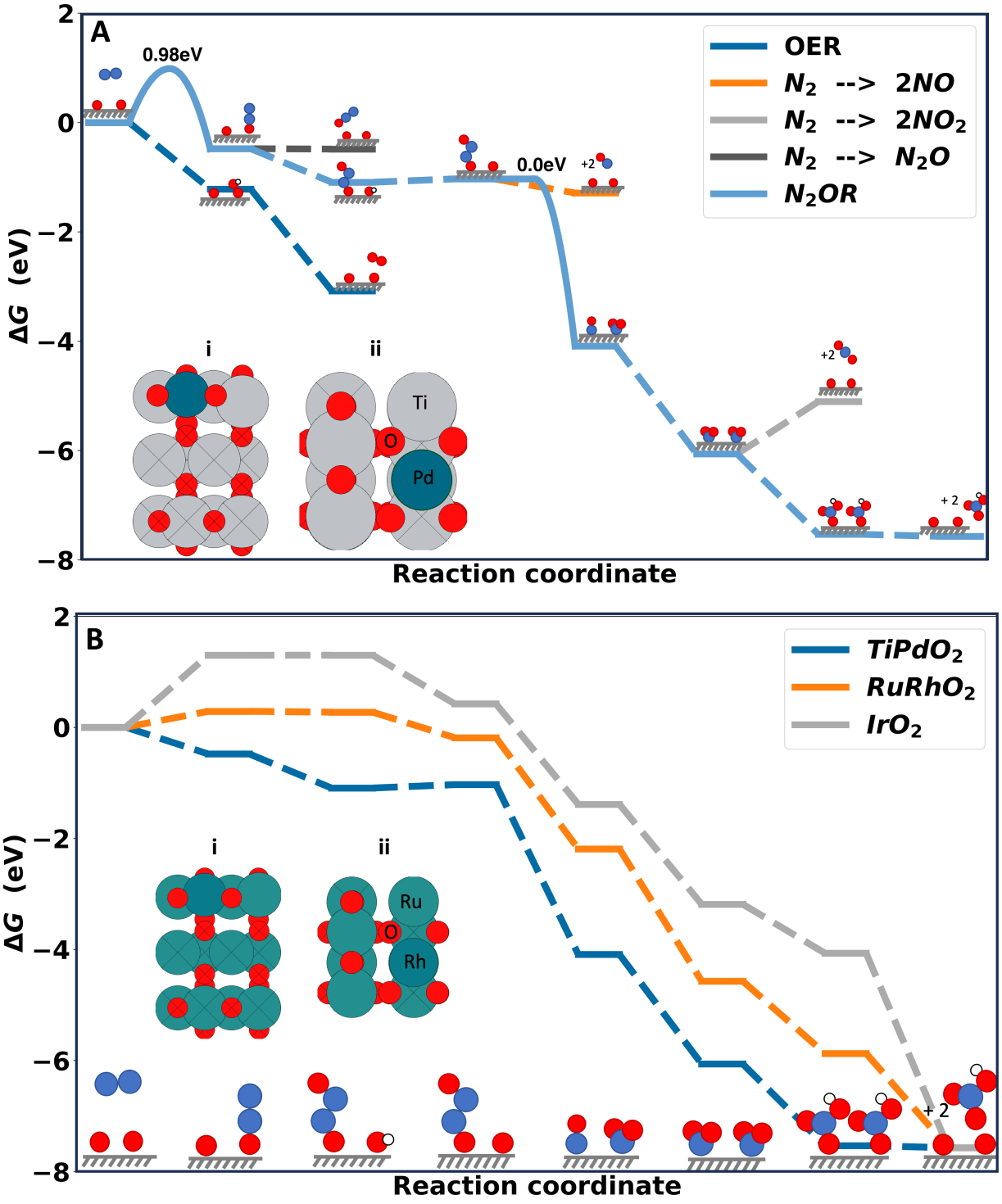

Figure 5: a) N_2 oxidation reaction mechanism at 2V vs RHE on $TiPdO_2$ (110) including possible side reactions. i) lateral and ii) top view of $TiPdO_2$ b) N_2 oxidation reaction mechanism at 2V vs RHE on three different rutile oxides. i) lateral and ii) top view of $RuRhO_2$

The free energy diagram includes reaction steps that are mostly electrochemical and involve coupled proton and electron transfer (CPET) in aqueous media. The barriers for such CPET steps have been found to be small ($<< 0.75$eV)[67] and also reduce with increasing applied potential. So, it is expected that the rate-limiting steps are the nonelectrochemical steps, which include the N_2 adsorption step ($N_2 + *O \longrightarrow *ON_2$) and the N-N bond breaking step. We calculated the N_2 adsorption barrier on TiPdO2 ($\Delta E_a^{*ON_2} = 0.98$ eV). This value is close to the previously calculated value of the same step on TiO2 ($\Delta E_a^{*ON_2} = 0.84$ eV).[51] The N-N bond-breaking step was calculated to be approximately barrierless because of the weakened N-N bond after binding to two oxygen atoms. At 2V vs RHE all the steps of the N2OR reaction are exergonic except for the oxidation of *OH to *O ($*OH \longrightarrow *O + (H^+ + e^-)$) which is slightly endergonic on this catalyst. Therefore, the formation of surface oxygen can possibly be a rate-limiting step at lower potentials ($<$ 2V vs RHE). The side reactions are shown to be thermodynamically less favorable compared to N2OR, except for OER, which is predicted to dominate at such potential (2V vs RHE) in aqueous electrolytes. OER dominates because of its more exergonic *OOH formation step and its faster kinetics at such potentials.

Our results suggest that limiting the OER activity is critical to improving N2OR selectivity. Some promising strategies to limit OER include using a non-aqueous solvent, which reduces access to proton acceptors and slows down the hydroxylation (and CPET) steps in the reaction. The rate of N2OR may be improved by increasing the partial pressure of N_2 during the reaction, which would increase the thermodynamic driving force towards N_2 adsorption.[68,69] Finally, alternating between a low and high potential at some optimum frequency may improve the selectivity towards N2OR.[70–72] Switching potential can limit the rate of the CPET steps because, at the lower potential, the system does not have enough driving force to complete OER steps, while the slow N_2 adsorption step is less affected by the potential change and our analysis suggests N_2 adsorption is more favored at low applied bias.

To investigate the viability of N2OR on different materials, we calculated the reaction energy of each step on the N2OR MvK mechanism on other rutile oxides and bimetallic oxides. Figure 5B shows the N2OR energy diagram on IrO2, RuRhO2 and TiPdO2 at 2V vs RHE. The N_2 adsorption step on IrO2 is very endergonic, making it less likely to adsorb N_2 to the surface oxygen, while on RuRhO2 it is slightly endergonic. By calculating the reaction energy of each step on the N2OR MvK mechanism on a number of rutile oxides (and bimetallics), we observed that the rate-limiting step for N2OR changes with operating potential. At lower applied potential (<1.23V vs RHE) the reaction is limited by the CPET steps while at higher potentials (>2V vs RHE) it is most likely limited by the non-electrochemical N_2 adsorption step. To improve our understanding of the activity trends on rutile oxides (and bimetallics), using the calculated reaction energies of each step of the two major competing reactions (OER and N2OR), we develop a limiting potential activity volcano shown in Figure 6.

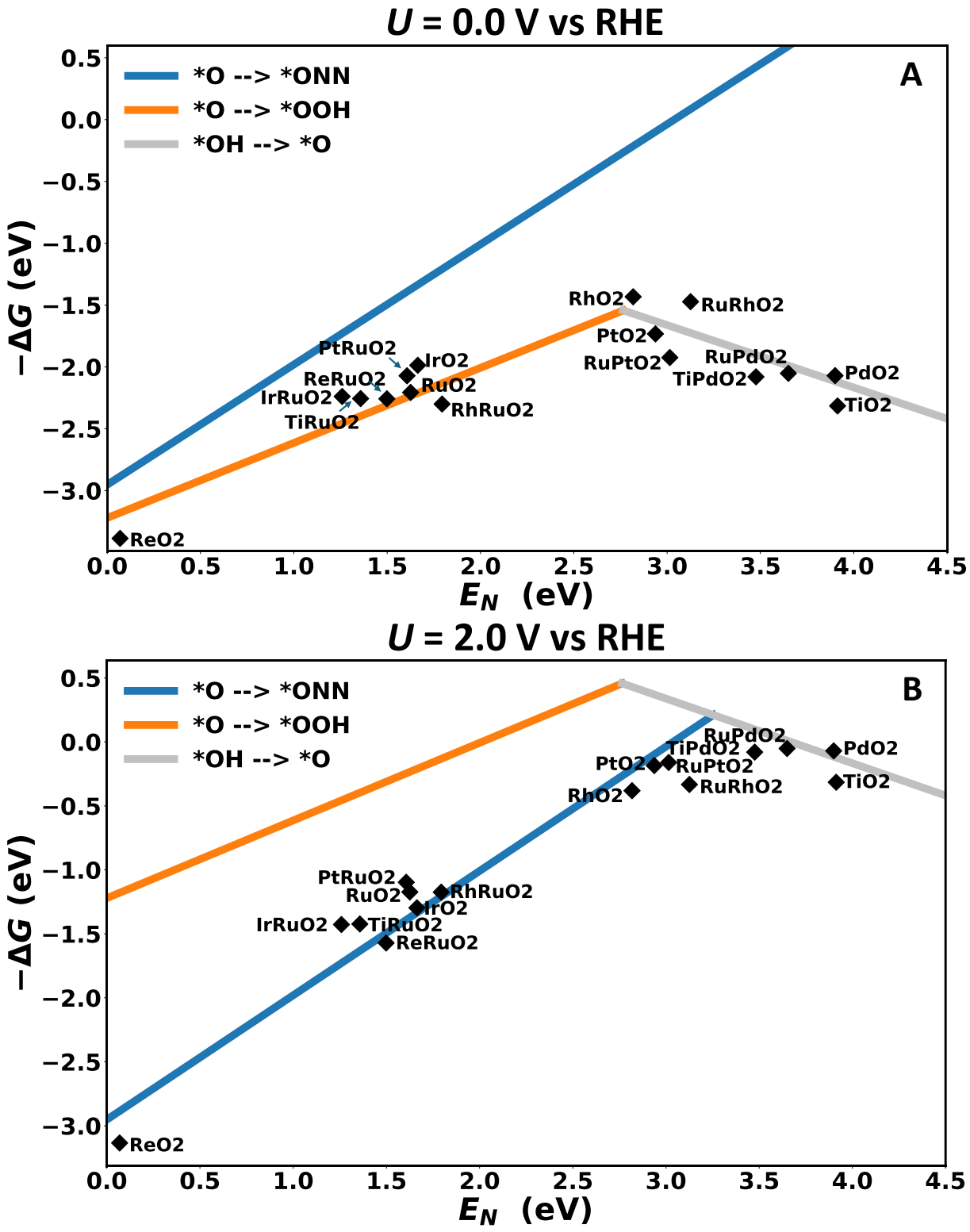

Figure 6: Limiting potential N2OR volcano plot shown at an applied bias of a) 0V vs RHE and b) 2V vs RHE.

Since the rate-limiting step changes with the operating potential, $\Delta G_{*ONN} - G_{*O}$ is largely independent of potential while $\Delta G_{*O} - G_{*OH}$ is highly dependent on potential, we expect a shift in the volcano peak with potential. Therefore, we show the calculated volcano at both $U = 0$ and $U = 2$V vs RHE, illustrated in Figure 6 using atomic nitrogen adsorption energy (ΔE_N) as the descriptor. The volcano plot shows that at 2V vs RHE, for N2OR reaction, the two most challenging steps from the weak and strong leg of the volcano are the formation of surface oxygen for weaker binding materials and N_2 adsorption to the surface oxygen for stronger binding materials. PdO2, PtO2, RuRhO2, TiPdO2, TiO2 and other bimetallic oxides of Ti,Pd and Ru can be good candidates for N2OR but in all cases, the activity of N2OR is dominated by OER. It is important to note that the left leg of the N2OR volcano is below the OER volcano suggesting that OER will thermodynamically take precedence on strong and moderately strong binding rutile oxides. While on the right leg, both OER and N2OR share a similar limiting step implying that OER will at least be as active as N2OR on weak binding rutile oxides. In the case where the two competing reactions share a similar thermodynamic limiting step, the selectivity will be highly dependent on the kinetics of each competing reaction. Ultimately, OER activity will outcompete N2OR activity at higher operating potential even on the right leg of the volcano plot because of the faster kinetics of OER when compared to N2OR where the moderately high activation barrier for N_2 adsorption ($N_2 + *O \longrightarrow *ON_2$ $\Delta E_a^{*ON_2} > 0.75$ eV) is not dependent on the operating potential. These findings of OER dominance on the anodic N_2 activation are similar to the dominance of HER on the cathodic N_2 activation[73,74]

Measurement of Catalytic Activity towards N2OR

Different oxide catalyts surfaces (PtO_2, PdO_2, RuO_4, TiO_2, TiO_2/PdO_2, TiO_2/RuO_2) were experimentally tested for N_2 oxidation activity. The choice of catalysts is based on the results of DFT calculations and the stability of catalysts at neutral pH in oxidation conditions. The

catalysts were tested at four different applied potentials- 1) static potentials (a. 2 V vs. RHE and b. 2.5 V vs. RHE) and 2) switching potentials (c. 2 s, 2 V vs. RHE ; 2 s, 1.3 V vs. RHE and d. 2 s, 2.5 V vs. RHE ; 2 s, 1.3 V vs. RHE). A switching potential approach was employed to limit the activity of OER (and all CPET steps) at the lower potential because the proposed rate-limiting step of N2OR is a non-CPET step. This approach was employed to improve the nitrate selectivity of N2OR as suggested by DFT. Figure 7 denotes the product Faradaic efficiencies (FE) for the N_2 oxidation on different catalyst surfaces at various applied potentials.

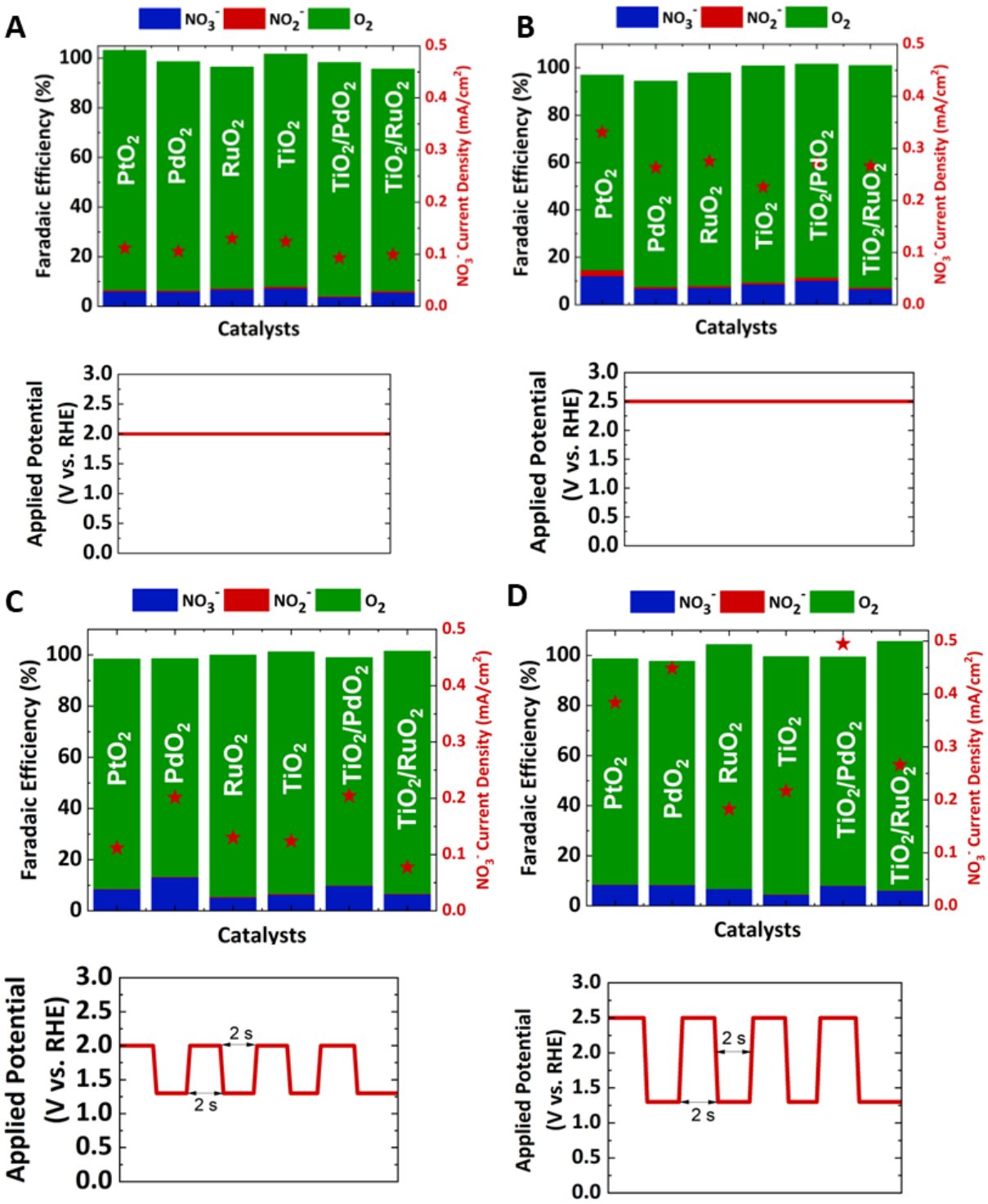

Figure 7: Faradaic efficiency of products on different catalyst surfaces at static potential a) 2 V vs RHE b) 2.5 V vs RHE, and switching potentials c) 2s, 2 V; 2s, 1.3 V vs. RHE d) 2s, 2.5 V ; 2s, 1.3 V vs. RHE.

In general, the catalysts are more active for oxygen evolution reaction (OER) at all the tested conditions with > 90 % FE, as predicted by theory. The selectivity towards NO_2^- is found to be negligible. The stability of NO_2^- is poor in oxidation conditions, and as such the formed NO_2^- could have been oxidized to NO_3^- in solution. We observe mostly NO_3^- post electrolysis. Overall, the N_2 oxidation activity is poor with < 10 % NO_3^- FE. The observed NO_3^- current density is higher on PdO_2 and TiO_2/PdO_2, which is in agreement with the developed theoretical activity volcano. PtO_2 exhibits the highest NO_3^- FE at a static potential of 2.5 V vs. RHE followed by TiO_2/PdO_2. Other catalyst surfaces such as PdO_2, RuO_4, TiO_2 and TiO_2/RuO_4 exhibit similar activity towards N_2 oxidation. When the potentials are switched between 2/2.5 V vs. RHE and 1.3 V vs. RHE, PdO_2 exhibited higher NO_3^- FE followed by TiO_2/PdO_2.

Figure 8A shows the NO_3^- current density as a function of the N_2 partial pressure on TiO_2/PdO_2 when the potentials are switched between 2.5 V and 1.3 V vs. RHE for 2 s each. The NO_3^- current density increases linearly when the N_2 partial pressure is increased and the estimated order of the reaction is 1, suggesting a rate-determining step involving N_2(g), in support of theoretical predictions of N_2 being involved in the rate-determining step. Figure 8B shows the NO_3^- current density as a function of applied potential on TiO_2/PdO_2 surface. Here, we observe non-Tafel (i.e., non-exponential) dependence of the current density on the applied bias, further supporting theoretical predictions of a non-CPET step being involved in the rate-determining step. These two results, taken together, strongly support N_2 adsorption as a rate-determining step for this process.

Figure 8C denotes the N-15 NMR spectra showing the peak corresponding to N-15 NO_3^- when N2 oxidation is performed on TiO_2/PdO_2 surface at 2.5 V vs. RHE confirming that the NO_3^- is produced by the electrochemical oxidation of N_2 as opposed to oxidation of background contaminants, such as ammonia. Overall, based on the experimental results the N_2 oxidation is extremely challenging in aqueous media and the activity could be increased by electrolyte engineering and the discovery of new high entropy alloys that can activate N_2.

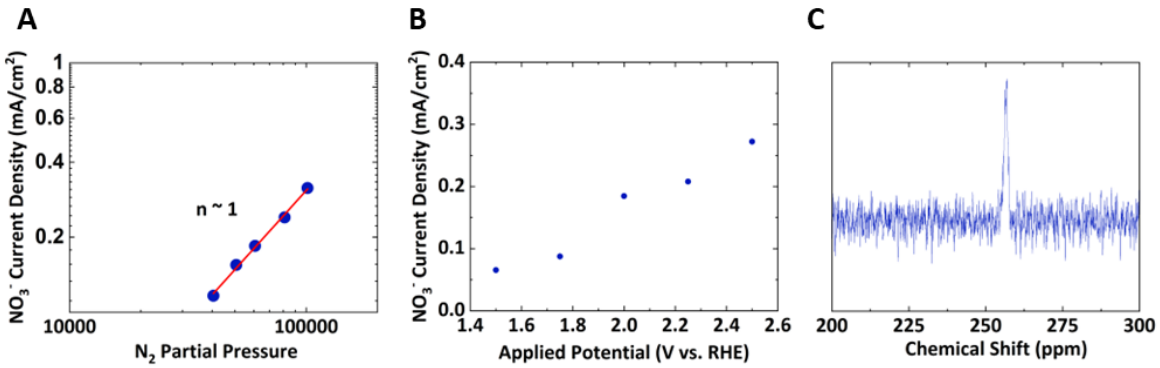

Figure 8: A) NO_3^- current density as a function of N_2 partial pressure on TiO_2/PdO_2 surface at 2.5 V vs. RHE. B) NO_3^- current density as a function of applied potential on TiO_2/PdO_2 surface C) N-15 NMR spectra for N_2 oxidation reaction on TiO_2/PdO_2 surface at 2.5 V vs. RHE.

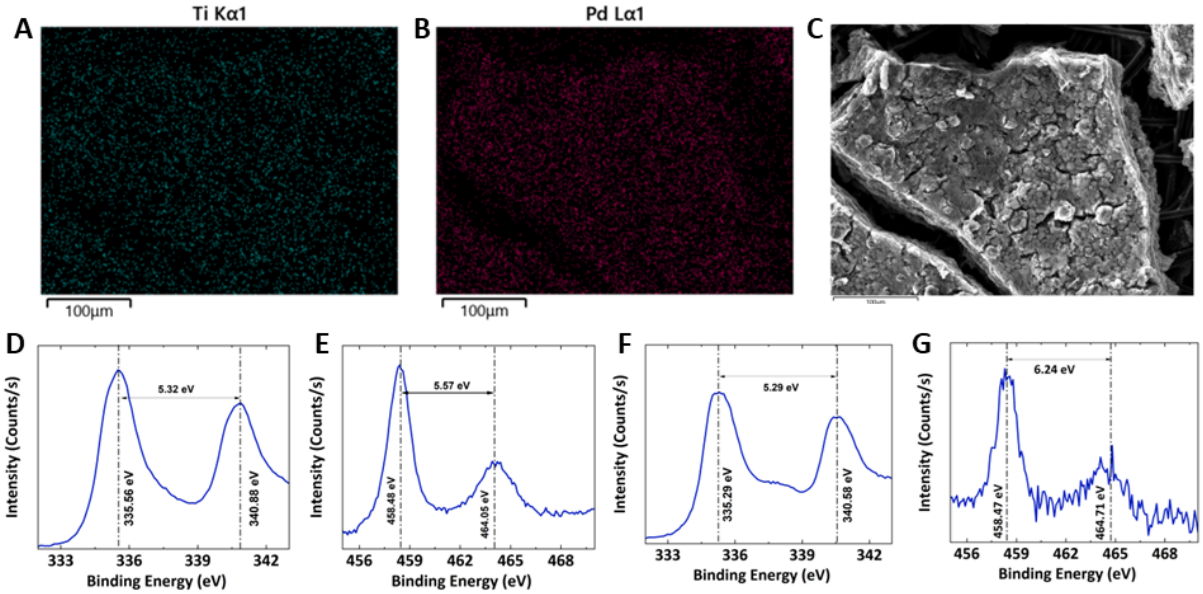

Figure 9: A) EDX Spectra showing the distribution of Ti. B) EDX Spectra showing the distribution of Pd. C) SEM image of the TiO_2/PdO_2 surface. D) XPS-HR scans of Pd-3d for pre electrolysis sample (TiO_2/PdO_2 surface) E) XPS-HR scans of Ti-2p for pre electrolysis sample (TiO_2/PdO_2 surface) F) XPS-HR scans of Pd-3d for post electrolysis sample (TiO_2/PdO_2 surface) G) XPS-HR scans of Ti-2p for post electrolysis sample (TiO_2/PdO_2 surface)

Catalyst characterization was performed to get a qualitative understanding of the nature of the catalyst. Figures 9A to 9C show the EDX and SEM image showing the distribution of Ti and Pd on the catalyst surface. Figures 9D and 9E show the XPS-HR scans of Pd-3d

and Ti-2p on the pre-electrolysis sample of TiO_2/PdO_2 surface. The binding energy peak at 340.88 eV ($3d_{5/2}$) corresponds to the +4 oxidation state of Pd, whereas the binding energy peak at 459 eV ($2p_{3/2}$) corresponds to the +4 oxidation state of Ti.[75] Figures 9F and 9G show the XPS-HR scans of Pd-3d and Ti-2p on the post-electrolysis sample of TiO_2/PdO_2 surface. There is a slight shift in binding energies for Pd, and Ti. It is difficult to attribute the reason for the shift as the analysis is done ex-situ. However, the oxidation states of the material do not change significantly post-electrolysis.

Conclusions

Electrochemical N_2 activation has proven challenging both on the anode and the cathode due to the inertness and strong triple bond in N_2, and the dominant water splitting reaction in aqueous media. In this work, we considered several mechanisms for anodic N_2 activation and discussed the limitations of each possible mechanism. We investigated the competitive adsorption of N_2 and OH on transition metal oxides and found that at N2OR operating conditions ($U > 1.24$ V vs RHE), the surface coverage of N_2 on metal sites will likely be extremely low compared to OH (and other OER intermediates in a reactive system). Similarly, a dissociative adsorption mechanism was found to be limited by availability of free metal sites and the high N-N bond dissociation energy of N_2. We developed a MvK mechanism pathway for N2OR on rutile oxides and calculated the energy barriers for critical non-electrochemical steps. On strong binding materials the first non-electrochemical step (N_2 adsorption) is endergonic, but becomes exergonic on weaker binding materials. N_2 adsorption via the MvK mechanism was found to be energetically less favorable than the corresponding OER step at operating conditions and has a relatively higher and potential independent barrier($E_a >$ 0.9 eV) compared to the corresponding OER step. Our thermodynamic analysis suggested dynamic potential control as a possible pathway to improve N2OR activity. Experimental analysis confirmed that most materials favor the OER pathway, and that dynamic potential

control can improve activity. The FE for N2OR is less than 10%, while the FE for the OER is greater than 90% on all materials used. The NO_3^- current density ranges from 0.06 to 0.26 mA/cm^2, influenced by both the applied potential and the N_2 partial pressure. The TiO2/PdO2 catalyst exhibits reasonable performance for OER, and moderate performance for N2OR. Based on the discussions in this work, future efforts to improve the selectivity and activity of N2OR should include optimizing the amplitude and frequency of dynamic potential control, operating at elevated N_2 partial pressure, improving catalyst design, or operating in water-deficient media (non-aqueous media).

Supporting Information

All geometry files used in the DFT analysis can be found as a supporting zip archive.

Notes

The authors declare no competing financial interest.

Conflict of Interest

The University of Illinois Chicago has filed a patent titled "Device and Methods for Production of Ammonia and Nitrates under Ambient Conditions" PCT/US2021/050573, WO/2022/060920, 2021

Acknowledgments

This material is based upon work supported by the National Science Foundation (NSF) Engineering Research Center for Advancing Sustainable and Distributed Fertilizer Production (CASFER) under Grant No. 2133576, in collaboration with the Materials and Systems Engineering Laboratory at the University of Illinois Chicago (UIC). Any opinions, findings, conclusions or recommendations expressed in this material are those of the author(s) and do not necessarily reflect the views of the National Science Foundation. This research used resources of the National Energy Research Scientific Computing Center (NERSC), a U.S. Department of Energy Office of Science User Facility located at Lawrence Berkeley Na-

tional Laboratory, operated under Contract No. DE-AC02-05CH11231 using NERSC award BES-ERCAP0022848. The authors acknowledge the High-Performance Computing Center (HPCC) at Texas Tech University for providing computational resources that have contributed to the research results reported within this paper. URL: http://www.hpcc.ttu.edu. . M.R.S. acknowledges funding support from UIC.

References

(1) Medford, A. J.; Hatzell, M. C. Photon-driven nitrogen fixation: current progress, thermodynamic considerations, and future outlook. *Acs Catalysis* **2017**, *7*, 2624–2643.

(2) Lim, J.; Fernández, C. A.; Lee, S. W.; Hatzell, M. C. Ammonia and nitric acid demands for fertilizer use in 2050. *ACS Energy Letters* **2021**, *6*, 3676–3685.

(3) Ostwald, W. Improvements in the manufacture of nitric acid and nitrogen oxides. *GBD190200698* **1902**, *19020109*.

(4) Ostwald, W. Improvements in and Relating to the Manufacture of Nitric Acid and Oxides of Nitrogen. *UK Patent GB* **1903**, *190208300*.

(5) Capdevila-Cortada, M. Electrifying the Haber–Bosch. *Nature Catalysis* **2019**, *2*, 1055–1055.

(6) Erisman, J. W.; Sutton, M. A.; Galloway, J.; Klimont, Z.; Winiwarter, W. How a century of ammonia synthesis changed the world. *Nature geoscience* **2008**, *1*, 636–639.

(7) Dybkjaer, I. *Ammonia: Catalysis and Manufacture*; Springer, 1995; pp 199–327.

(8) Li, J.; Xiong, Q.; Mu, X.; Li, L. Recent Advances in Ammonia Synthesis: From Haber-Bosch Process to External Field Driven Strategies. *ChemSusChem* **2024**, e202301775.

(9) Bora, N.; Singh, A. K.; Pal, P.; Sahoo, U. K.; Seth, D.; Rathore, D.; Bhadra, S.; Sevda, S.; Venkatramanan, V.; Prasad, S., et al. Green ammonia production: Process technologies and challenges. *Fuel* **2024**, *369*, 131808.

(10) Schrock, R. R. Catalytic reduction of dinitrogen to ammonia at a single molybdenum center. *Accounts of chemical research* **2005**, *38*, 955–962.

(11) Anderson, J. S.; Rittle, J.; Peters, J. C. Catalytic conversion of nitrogen to ammonia by an iron model complex. *Nature* **2013**, *501*, 84–87.

(12) Tong, X.; Benyuan, M.; Jie, L.; Luchao, Y.; Qian, L.; Tingshuai, L.; Haitao, Z.; Yonglan, L.; Siyu, L.; Xuping, S. Recent progress in metal-free electrocatalysts toward ambient N2 reduction reaction. *Acta Physico-Chimica Sinica* **2021**, *37*, 2009043–0.

(13) Van der Ham, C. J.; Koper, M. T.; Hetterscheid, D. G. Challenges in reduction of dinitrogen by proton and electron transfer. *Chemical Society Reviews* **2014**, *43*, 5183–5191.

(14) Shen, H.; Choi, C.; Masa, J.; Li, X.; Qiu, J.; Jung, Y.; Sun, Z. Electrochemical ammonia synthesis: mechanistic understanding and catalyst design. *Chem* **2021**, *7*, 1708–1754.

(15) Li, Y.; Zhang, Q.; Mei, Z.; Li, S.; Luo, W.; Pan, F.; Liu, H.; Dou, S. Recent advances and perspective on electrochemical ammonia synthesis under ambient conditions. *Small Methods* **2021**, *5*, 2100460.

(16) Xu, T.; Liang, J.; Wang, Y.; Li, S.; Du, Z.; Li, T.; Liu, Q.; Luo, Y.; Zhang, F.; Shi, X., et al. Enhancing electrocatalytic N2-to-NH3 fixation by suppressing hydrogen evolution with alkylthiols modified Fe3P nanoarrays. *Nano Research* **2022**, *15*, 1039–1046.

(17) Mao, S.; Duan, Z. A thermodynamic model for calculating nitrogen solubility, gas phase composition and density of the N2–H2O–NaCl system. *Fluid phase equilibria* **2006**, *248*, 103–114.

(18) Kani, N. C.; Prajapati, A.; Collins, B. A.; Goodpaster, J. D.; Singh, M. R. Competing effects of pH, cation identity, H2O saturation, and N2 concentration on the activity and selectivity of electrochemical reduction of N2 to NH3 on electrodeposited Cu at ambient conditions. *ACS Catalysis* **2020**, *10*, 14592–14603.

(19) Choi, J.; Suryanto, B. H.; Wang, D.; Du, H.-L.; Hodgetts, R. Y.; Ferrero Vallana, F. M.; MacFarlane, D. R.; Simonov, A. N. Identification and elimination of false positives in electrochemical nitrogen reduction studies. *Nature communications* **2020**, *11*, 5546.

(20) Andersen, S. Z.; Čolić, V.; Yang, S.; Schwalbe, J. A.; Nielander, A. C.; McEnaney, J. M.; Enemark-Rasmussen, K.; Baker, J. G.; Singh, A. R.; Rohr, B. A., et al. A rigorous electrochemical ammonia synthesis protocol with quantitative isotope measurements. *Nature* **2019**, *570*, 504–508.

(21) Tsuneto, A.; Kudo, A.; Sakata, T. Efficient electrochemical reduction of N2 to NH3 catalyzed by lithium. *Chemistry letters* **1993**, *22*, 851–854.

(22) Tsuneto, A.; Kudo, A.; Sakata, T. Lithium-mediated electrochemical reduction of high pressure N2 to NH3. *Journal of Electroanalytical Chemistry* **1994**, *367*, 183–188.

(23) Du, H.-L.; Chatti, M.; Hodgetts, R. Y.; Cherepanov, P. V.; Nguyen, C. K.; Matuszek, K.; MacFarlane, D. R.; Simonov, A. N. Electroreduction of nitrogen with almost 100% current-to-ammonia efficiency. *Nature* **2022**, *609*, 722–727.

(24) Li, K.; Andersen, S. Z.; Statt, M. J.; Saccoccio, M.; Bukas, V. J.; Krempl, K.; Sažinas, R.; Pedersen, J. B.; Shadravan, V.; Zhou, Y., et al. Enhancement of lithium-mediated ammonia synthesis by addition of oxygen. *Science* **2021**, *374*, 1593–1597.

(25) Westhead, O.; Tort, R.; Spry, M.; Rietbrock, J.; Jervis, R.; Grimaud, A.; Bagger, A.; Stephens, I. L. The origin of overpotential in lithium-mediated nitrogen reduction. *Faraday Discussions* **2023**,

(26) Gritzner, G. Standard electrode potentials of M+— M couples in non-aqueous solvents (molecular liquids). *Journal of Molecular Liquids* **2010**, *156*, 103–108.

(27) Kani, N. C.; Goyal, I.; Gauthier, J. A.; Shields, W.; Shields, M.; Singh, M. R. Pathway toward Scalable Energy-Efficient Li-Mediated Ammonia Synthesis. *ACS Applied Materials & Interfaces* **2024**, *16*, 16203–16212.

(28) Cai, X.; Li, X.; You, J.; Yang, F.; Shadike, Z.; Qin, S.; Luo, L.; Guo, Y.; Yan, X.; Shen, S., et al. Lithium-mediated ammonia electrosynthesis with ether-based electrolytes. *Journal of the American Chemical Society* **2023**, *145*, 25716–25725.

(29) Fu, X.; Li, S.; Deissler, N. H.; Mygind, J. B. V.; Kibsgaard, J.; Chorkendorff, I. Effect of Lithium Salt on Lithium-Mediated Ammonia Synthesis. *ACS Energy Letters* **2024**, *9*, 3790–3795.

(30) Sazinas, R.; Li, K.; Andersen, S. Z.; Saccoccio, M.; Li, S.; Pedersen, J. B.; Kibsgaard, J.; Vesborg, P. C.; Chakraborty, D.; Chorkendorff, I. Oxygen-enhanced chemical stability of lithium-mediated electrochemical ammonia synthesis. *The Journal of Physical Chemistry Letters* **2022**, *13*, 4605–4611.

(31) Goyal, I.; Kani, N. C.; Olusegun, S. A.; Chinnabattigalla, S.; Bhawnani, R. R.; Glusac, K. D.; Singh, A. R.; Gauthier, J. A.; Singh, M. R. Metal Nitride as a Mediator for the Electrochemical Synthesis of NH3. *ACS Energy Letters* **2024**, 4188–4195.

(32) Fu, X.; Niemann, V. A.; Zhou, Y.; Li, S.; Zhang, K.; Pedersen, J. B.; Saccoccio, M.; Andersen, S. Z.; Enemark-Rasmussen, K.; Benedek, P., et al. Calcium-mediated nitrogen reduction for electrochemical ammonia synthesis. *Nature Materials* **2024**, *23*, 101–107.

(33) Krebsz, M.; Hodgetts, R. Y.; Johnston, S.; Nguyen, C. K.; Hora, Y.; MacFarlane, D. R.; Simonov, A. N. Reduction of dinitrogen to ammonium through a magnesium-based electrochemical process at close-to-ambient temperature. *Energy & Environmental Science* **2024**, *17*, 4481–4487.

(34) Kani, N. C.; Gauthier, J. A.; Prajapati, A.; Edgington, J.; Bordawekar, I.; Shields, W.; Shields, M.; Seitz, L. C.; Singh, A. R.; Singh, M. R. Solar-driven electrochemical synthesis of ammonia using nitrate with 11% solar-to-fuel efficiency at ambient conditions. *Energy & Environmental Science* **2021**, *14*, 6349–6359.

(35) Fu, X.; Zhao, X.; Hu, X.; He, K.; Yu, Y.; Li, T.; Tu, Q.; Qian, X.; Yue, Q.; Wasielewski, M. R., et al. Alternative route for electrochemical ammonia synthesis by reduction of nitrate on copper nanosheets. *Applied Materials Today* **2020**, *19*, 100620.

(36) Chen, G.-F.; Yuan, Y.; Jiang, H.; Ren, S.-Y.; Ding, L.-X.; Ma, L.; Wu, T.; Lu, J.; Wang, H. Electrochemical reduction of nitrate to ammonia via direct eight-electron transfer using a copper–molecular solid catalyst. *Nature Energy* **2020**, *5*, 605–613.

(37) van Langevelde, P. H.; Katsounaros, I.; Koper, M. T. Electrocatalytic nitrate reduction for sustainable ammonia production. *Joule* **2021**, *5*, 290–294.

(38) Ren, T.; Yu, Z.; Yu, H.; Deng, K.; Wang, Z.; Li, X.; Wang, H.; Wang, L.; Xu, Y. Interfacial polarization in metal-organic framework reconstructed Cu/Pd/CuOx multi-phase heterostructures for electrocatalytic nitrate reduction to ammonia. *Applied Catalysis B: Environmental* **2022**, *318*, 121805.

(39) Fang, W.; Du, C.; Kuang, M.; Chen, M.; Huang, W.; Ren, H.; Xu, J.; Feldhoff, A.; Yan, Q. Boosting efficient ambient nitrogen oxidation by a well-dispersed Pd on MXene electrocatalyst. *Chemical Communications* **2020**, *56*, 5779–5782.

(40) Guo, Y.; Zhang, S.; Zhang, R.; Wang, D.; Zhu, D.; Wang, X.; Xiao, D.; Li, N.; Zhao, Y.; Huang, Z., et al. Electrochemical nitrate production via nitrogen oxidation with atomically dispersed Fe on N-doped carbon nanosheets. *ACS nano* **2021**, *16*, 655–663.

(41) Dai, C.; Sun, Y.; Chen, G.; Fisher, A. C.; Xu, Z. J. Electrochemical oxidation of nitrogen towards direct nitrate production on spinel oxides. *Angewandte Chemie International Edition* **2020**, *59*, 9418–9422.

(42) Kuang, M.; Wang, Y.; Fang, W.; Tan, H.; Chen, M.; Yao, J.; Liu, C.; Xu, J.; Zhou, K.; Yan, Q. Efficient nitrate synthesis via ambient nitrogen oxidation with Ru-doped TiO2/RuO2 electrocatalysts. *Advanced Materials* **2020**, *32*, 2002189.

(43) Han, S.; Wang, C.; Wang, Y.; Yu, Y.; Zhang, B. Electrosynthesis of Nitrate via the Oxidation of Nitrogen on Tensile-Strained Palladium Porous Nanosheets. *Angewandte Chemie* **2021**, *133*, 4524–4528.

(44) Li, T.; Han, S.; Wang, C.; Huang, Y.; Wang, Y.; Yu, Y.; Zhang, B. Ru-doped Pd nanoparticles for nitrogen electrooxidation to nitrate. *ACS Catalysis* **2021**, *11*, 14032–14037.

(45) Wang, Y.; Yu, Y.; Jia, R.; Zhang, C.; Zhang, B. Electrochemical synthesis of nitric acid from air and ammonia through waste utilization. *National Science Review* **2019**, *6*, 730–738.

(46) Zhang, L.; Cong, M.; Ding, X.; Jin, Y.; Xu, F.; Wang, Y.; Chen, L.; Zhang, L. A janus Fe-SnO2 catalyst that enables bifunctional electrochemical nitrogen fixation. *Angewandte Chemie* **2020**, *132*, 10980–10985.

(47) Zhang, Y.; Du, F.; Wang, R.; Ling, X.; Wang, X.; Shen, Q.; Xiong, Y.; Li, T.; Zhou, Y.; Zou, Z. Electrocatalytic fixation of N into NO: electron transfer between oxygen vacancies and loaded Au in NbO nanobelts to promote ambient nitrogen oxidation. **2021**,

(48) Lan, J.; Luo, M.; Han, J.; Peng, M.; Duan, H.; Tan, Y. Nanoporous B13C2 towards highly efficient electrochemical nitrogen fixation. *Small* **2021**, *17*, 2102814.

(49) Nie, Z.; Zhang, L.; Ding, X.; Cong, M.; Xu, F.; Ma, L.; Guo, M.; Li, M.; Zhang, L. Catalytic kinetics regulation for enhanced electrochemical nitrogen oxidation by Ru-nanoclusters-coupled Mn3O4 catalysts decorated with atomically dispersed Ru atoms. *Advanced Materials* **2022**, *34*, 2108180.

(50) Wan, H.; Bagger, A.; Rossmeisl, J. Limitations of electrochemical nitrogen oxidation toward nitrate. *The Journal of Physical Chemistry Letters* **2022**, *13*, 8928–8934.

(51) Anand, M.; Abraham, C. S.; Nørskov, J. K. Electrochemical oxidation of molecular nitrogen to nitric acid–towards a molecular level understanding of the challenges. *Chemical science* **2021**, *12*, 6442–6448.

(52) Long, J.; Luan, D.; Fu, X.; Li, H.; Jing, H.; Xiao, J. Fundamental Insights on the Electrochemical Nitrogen Oxidation over Metal Oxides. *ACS Catalysis* **2024**, *14*, 4423–4431.

(53) Wang, Y.; Li, T.; Yu, Y.; Zhang, B. Electrochemical synthesis of nitric acid from nitrogen oxidation. *Angewandte Chemie* **2022**, *134*, e202115409.

(54) Chen, S.; Liang, S.; Huang, R.; Zhang, M.; Song, Y.; Zhang, Y.; Tao, S.; Yu, L.; Deng, D. Direct electroconversion of air to nitric acid under mild conditions. *Nature Synthesis* **2024**, *3*, 76–84.

(55) Nørskov, J. K.; Rossmeisl, J.; Logadottir, A.; Lindqvist, L.; Kitchin, J. R.; Bligaard, T.; Jónsson, H. Origin of the Overpotential for Oxygen Reduction at a Fuel-Cell Cathode. *The Journal of Physical Chemistry B* **2004**, *108*, 17886–17892.

(56) Kresse, G.; Hafner, J. Ab initio molecular dynamics for liquid metals. *Physical Review B* **1993**, *47*, 558.

(57) Kresse, G.; Furthmüller, J. Efficiency of ab-initio total energy calculations for metals and semiconductors using a plane-wave basis set. *Computational Materials Science* **1996**, *6*, 15–50.

(58) Kresse, G.; Furthmüller, J. Efficient iterative schemes for ab initio total-energy calculations using a plane-wave basis set. *Physical Review B* **1996**, *54*, 11169.

(59) Larsen, A. H.; Mortensen, J. J.; Blomqvist, J.; Castelli, I. E.; Christensen, R.; Dułak, M.; Friis, J.; Groves, M. N.; Hammer, B.; Hargus, C. The atomic simulation environment—a Python library for working with atoms. *Journal of Physics: Condensed Matter* **2017**, *29*, 273002.

(60) Kresse, G.; Joubert, D. From ultrasoft pseudopotentials to the projector augmented-wave method. *Physical Review B* **1999**, *59*, 1758.

(61) Hammer, B.; Hansen, L. B.; Nørskov, J. K. Improved adsorption energetics within density-functional theory using revised Perdew-Burke-Ernzerhof functionals. *Physical Review B* **1999**, *59*, 7413.

(62) Mathew, K.; Sundararaman, R.; Letchworth-Weaver, K.; Arias, T.; Hennig, R. G. Implicit solvation model for density-functional study of nanocrystal surfaces and reaction pathways. *The Journal of Chemical Physics* **2014**, *140*, 084106.

(63) Mathew, K.; Kolluru, V. C.; Mula, S.; Steinmann, S. N.; Hennig, R. G. Implicit self-consistent electrolyte model in plane-wave density-functional theory. *The Journal of Chemical Physics* **2019**, *151*, 234101.

(64) Monkhorst, H. J.; Pack, J. D. Special points for Brillouin-zone integrations. *Physical Review B* **1976**, *13*, 5188.

(65) Lee, E. M.; Ludwig, T.; Yu, B.; Singh, A. R.; Gygi, F.; Nørskov, J. K.; de Pablo, J. J. Neural network sampling of the free energy landscape for nitrogen dissociation on ruthenium. *The Journal of Physical Chemistry Letters* **2021**, *12*, 2954–2962.

(66) Griess, P. Preliminary notice of the reaction of nitrous acid with picramic acid and aminonitrophenol. *Annalen der Chemie und Pharmacie* **1858**, 123–125.

(67) Dickens, C. F.; Kirk, C.; Nørskov, J. K. Insights into the electrochemical oxygen evolu-

tion reaction with ab initio calculations and microkinetic modeling: beyond the limiting potential volcano. *The Journal of Physical Chemistry C* **2019**, *123*, 18960–18977.

(68) Kani, N. C.; Olusegun, S.; Chauhan, R.; Gauthier, J. A.; Singh, M. R. High-pressure electrochemistry: a new frontier in decarbonization. *EES Catalysis* **2024**, *2*, 507–521.

(69) Giovanelli, D.; Lawrence, N. S.; Compton, R. G. Electrochemistry at high pressures: A review. *Electroanalysis: An International Journal Devoted to Fundamental and Practical Aspects of Electroanalysis* **2004**, *16*, 789–810.

(70) Vempatti, V. V. R.; Wang, S.; Abdelrahman, O. A.; Dauenhauer, P. J.; Grabow, L. C. Accelerated Steam Methane Reforming by Dynamically Applied Charges. *The Journal of Physical Chemistry C* **2024**,

(71) Qi, J.; Resasco, J.; Robatjazi, H.; Alvarez, I. B.; Abdelrahman, O.; Dauenhauer, P.; Christopher, P. Dynamic control of elementary step energetics via pulsed illumination enhances photocatalysis on metal nanoparticles. *ACS Energy Letters* **2020**, *5*, 3518–3525.

(72) Andersen, S. Z.; Statt, M. J.; Bukas, V. J.; Shapel, S. G.; Pedersen, J. B.; Krempl, K.; Saccoccio, M.; Chakraborty, D.; Kibsgaard, J.; Vesborg, P. C., et al. Increasing stability, efficiency, and fundamental understanding of lithium-mediated electrochemical nitrogen reduction. *Energy & Environmental Science* **2020**, *13*, 4291–4300.

(73) Montoya, J. H.; Tsai, C.; Vojvodic, A.; Nørskov, J. K. The challenge of electrochemical ammonia synthesis: a new perspective on the role of nitrogen scaling relations. *ChemSusChem* **2015**, *8*, 2180–2186.

(74) Singh, A. R.; Rohr, B. A.; Schwalbe, J. A.; Cargnello, M.; Chan, K.; Jaramillo, T. F.; Chorkendorff, I.; Nørskov, J. K. Electrochemical Ammonia Synthesis The Selectivity Challenge. 2017.

(75) Chastain, J.; King Jr, R. C. Handbook of X-ray photoelectron spectroscopy. *Perkin-Elmer Corporation* **1992**, *40*, 221.